Journal of The Electrochemical Society, **152** (6) E193-E199 (2005)
0013-4651/2005/152(6)/E193/7/$7.00 © The Electrochemical Society, Inc.

Potential Shift for OH(ads) Formation on the Pt Skin on $Pt_3Co(111)$ Electrodes in Acid

Theory and Experiment

Jérôme Roques,[a] Alfred B. Anderson,[a,*,z] Vivek S. Murthi,[b] and Sanjeev Mukerjee[b,*]

[a]*Department of Chemistry, Case Western Reserve University, Cleveland, Ohio 44106-7078, USA*
[b]*Department of Chemistry, Northeastern University, Boston, Massachusetts 02115-5000, USA*

A study combining theoretical predictions and experimental measurements was made to gain an understanding of the beneficial effect of alloying cobalt into platinum for electroreduction of oxygen. Carbon-supported Pt_3Co catalyst particles were characterized by X-ray diffraction spectroscopy and X-ray absorption near-edge structure, which gave evidence for a surface layer composed of Pt, called the Pt skin. Electrochemical measurements were made in 1 M trifluoromethane sulfonic acid with a rotating ring disk setup. Cyclic voltammetry showed significantly less oxide formation in the >0.8 V range over the skin on the alloy compared to nonalloyed Pt. Tafel plots showed a 50-70 mV reduction in overpotential for O_2 reduction over the Pt skin. The Vienna Ab Initio Simulation Program was used for calculating H_2O and OH adsorption bond strengths on the Pt skin on $Pt_3Co(111)$ for comparison with prior work with the Pt(111) surface. The bond strength variations were used to estimate the shift in reversible potential for OH_{ads} formation from H_2O_{ads} oxidation. A shift of 80 mV was found, which indicates that an increase in the reversible potential for OH_{ads} formation correlates with the decrease in overpotential for O_2 reduction over the Pt skin on Pt_3Co nanoparticles.
 [DOI: 10.1149/1.1896328]

Manuscript submitted July 9, 2004; revised manuscript received October 22, 2004. Available electronically April 18, 2005.

The main reactions involved at each of the fuel cell electrodes are the reduction of oxygen to water and the oxidation of hydrogen. The poor kinetics of oxygen reduction are largely responsible for the decrease of the fuel cell efficiency.[1] In the past few years, considerable attention has been given to developing an understanding of the oxygen reduction reaction (ORR) on Pt surfaces. Theoretical studies from the Anderson laboratory suggest that a series pathway via an H_2O_2(ads) intermediate may be operative on Pt catalysts when only onefold surface sites are available[2]

$$\text{Pt-OH}_2 + \text{O}_2 \rightarrow \text{Pt-O}_2 + \text{H}_2\text{O} \quad [1]$$

$$\text{Pt-O}_2 + \text{H}^+_{aq} + \text{e}^-(U) \rightarrow \text{Pt-OOH} \quad [2]$$

$$\text{Pt-OOH} + \text{H}^+_{aq} + \text{e}^-(U) \rightarrow \text{Pt-(OHOH)} \quad [3]$$

$$\text{Pt-(OHOH)} + \text{H}^+_{aq} + \text{e}^-(U) \rightarrow \text{Pt-OH} + \text{H}_2\text{O} \quad [4]$$

$$\text{Pt-OH} + \text{H}^+_{aq} + \text{e}^-(U) \rightarrow \text{Pt-OH}_2 \quad [5]$$

In these equations U is the electrode potential. More recently, it was shown that Pt-OOH can dissociate if formed over a twofold surface site, leading to the mechanism[3]

$$\text{O}_2(\text{di-}\sigma) + \text{H}^+_{aq} + \text{e}^-(U) \rightarrow \text{OOH(di-}\sigma) \quad [6]$$

$$\text{OOH(di-}\sigma) \rightarrow \text{O(bridging)} + \text{OH(onefold)} \quad [7]$$

$$\text{O(bridging)} + \text{OH(onefold)} + 3\text{H}^+_{aq} + 3\text{e}^-(U) \rightarrow 2\text{H}_2\text{O} \quad [8]$$

The standard reversible potential for O_2 reduction in H_2O is 1.23 V on the standard hydrogen scale [standard hydrogen electrode (SHE)]. However, due to kinetic effects, an oxygen cathode in a fuel cell has a working potential of around 0.8 V. A contributing factor in the $\sim$400 mV overpotential is believed to be the formation of molecular species at around 0.8 V that blocks the bonding of O_2 to the catalytically active surface sites.[1,4,5] It is thought that in acid solution OH_{ads} is formed from oxidation of water on platinum surfaces at around 0.7 V and that the OH_{ads} blocks surface sites for O_2 adsorption[1,6]

$$\text{H}_2\text{O}_{ads} \rightarrow \text{OH}_{ads} + \text{H}^+_{aq} + \text{e}^-(U) \quad [9]$$

Several investigations have been carried out recently with the goal of improving the electrocatalytic activity of platinum cathodes for the ORR. To this end, metal alloys composed of two or more metals have often been employed.[1,4,7-10] Mukerjee *et al.*[4,9] investigated five carbon-supported binary Pt alloys nanoparticles and found enhanced electrocatalytic activity for the ORR on them compared to Pt/C electrocatalysts. Stamenkovic *et al.*[5] studied the ORR on polycrystalline Pt and on Pt_3Ni and Pt_3Co alloy electrode surfaces in acid electrolytes, using the rotating ring disk electrode method. Their alloy surfaces were prepared in ultrahigh vacuum, and two different surface compositions were made. In one the first layer had 75% Pt and 25% Ni or Co (mixed metal surface), and the other had 100% Pt in the first layer (called the Pt skin). They observed that Pt_3Ni and Pt_3Co alloy surfaces, both in the presence and absence of the Pt skin, had improved electrocatalytic activity for the ORR relative to Pt/C electrocatalysts. Roques and Anderson recently made a periodic spin-density-functional theory study of the annealed Pt_3Cr alloy surface (with a Pt skin on the top of the alloy) for comparison with Pt(111).[11] They calculated OH and H_2O adsorption bond strengths. Using a model based on reaction energy changes, they then calculated a 0.11 V positive shift in the reversible potential of OH_{ads} formation from H_2O_{ads} in acid solution. This result suggested that the $\sim$0.06 V positive shift of the onset potential for surface oxidation obtained experimentally by Uribe and Zawodzinski[10] and the $\sim$0.05 V positive shift in the O_2 reduction potential (*i.e.*, a decrease in overpotential) for Pt_3Cr carbon-supported alloy observed by Mukerjee *et al.*[4] could be due to reduced OH_{ads} coverage on the alloys relative to pure Pt.

In this work, the effects of alloying Pt with Co are studied theoretically and experimentally. The manuscript is divided in three parts: the first part presents experimental results; the second part presents theoretical results, and the third part is an overall conclusion about the Pt_3Co effect on the reversible potential of OH_{ads} formation from H_2O_{ads} and its effect on the overpotential of O_2 reduction in H_2O_{ads}.

Experimental

Surface preparation and characterization.—Electrocatalyst.— When the 3d transition metal, M, is one of the elements V through Ni of the first transition, the ordered PtM alloys generally have a CuAu-type (or $L1_0$) tetragonal structure and the Pt_3M

* Electrochemical Society Active Member.
z E-mail: aba@po.cwru.edu

Table I. Results of XANES (at Pt L and K edge of alloying metal) and extended X-ray absorption fine structure (EXAFS) analyses (at Pt L_3 edge) for supported Pt and Pt alloy electrocatalysts. All data measured *in situ* at 0.54 V and 0.84 V *vs.* RHE.

		Electrode potential (0.54 V *vs.* RHE)			Electrode potential (0.84 V *vs.* RHE)		
Electrocatalyst	Atomic ratio (atom %) XANES	$(h_j)_{t,s}$ Pt d-band vacancy	Pt-Pt (Å)	Pt-Pt (N)	$(h_j)_{t,s}$ Pt d-band vacancy	Pt-Pt (Å)	Pt-Pt (N)
Pt/C	-	0.329	2.77	8.7	0.370	2.77	6.8
PtCo/C	72/28	0.401	2.68	6.9	0.390	2.68	7.6

Windows for the Fourier transform parameters used for EXAFS analysis of Pt L_3 edge at 0.54 V are as follows: Pt/C: $k^n = 3$; Δk (Å^{-1}) = 3.49-14.23; Δr (Å) = 1.4-3.05. PtCo/C: $k^n = 3$; Δk (Å^{-1}) = 3.22-14.61; Δr (Å) = 1.5-3.5.

and PtM_3 alloys usually have a Cu_3Au-type (or $L1_2$) face-centered cubic (fcc) structure. Recently, Mukerjee *et al.*[12] used X-ray diffraction (XRD) to study the binary Pt alloys PtCr/C, PtMn/C, PtFe/C, PtCo/C, and PtNi/C supported on high surface area carbon. They found that at room temperature all the alloys were Pt_3M and they exhibited a high degree of crystallinity in the $L1_2$-type lattice. A secondary phase of the type PtM possessing an $L1_0$-type lattice was also seen. However, based on diffraction line intensities, this phase was estimated to make a minor contribution (from 3 to 9% of the alloy composition). Therefore, in this work, we have assumed the Pt_3Co alloy composition in analyzing the spectroscopic measurements and in making the quantum mechanical studies. Pt/C catalysts were used for comparison of results. All electrocatalysts were made in-house using well-known colloidal "sol" and carbothermic reduction methods.[13-19] The metal loading on the carbon support (Vulcan XC-72, Cabot, USA) was 20%. In the synthesis, an oxide of the second alloying element was deposited on the supported Pt/C electrocatalyst and then subjected to carbothermic reduction at 900°C under inert conditions. This yielded supported alloy nanoparticles.

Electrode preparation.—A catalyst suspension with a concentration of 1 mg catalyst in 1 mL isopropanol was prepared using ultrasonication. A small amount of Nafion was added to the catalyst suspension to act as a binder. The loading used was very small relative to normal fuel cell electrodes (wt ratio of Pt/C to Nafion 50:1, mg/cm^2) but comparable to loadings used in rotating disk electrode (RDE) experiments reported recently.[20-23] A finely polished glassy carbon (GC) disk electrode (0.283 cm^2, Pine Instruments) was used as the substrate for the supported catalysts. A 20 μL aliquot containing 4 μg of metal was taken from the initial suspension using a micropipette and loaded on the GC to give a constant metal loading of ~14 μg/cm^2. The electrode was then allowed to dry at room temperature before introducing it into the electrolyte. The adhesion of the catalysts to the GC was verified both visibly and by cyclic voltammetry by observing hydrogen adsorption-desorption features. After 50 cycles at 50 mV/s, the electrodes were further cycled at 10 mV/s for 10 cycles.

RDE measurements.—The electrode was immersed in oxygen-free 1 M trifluoromethane sulfonic acid (TFMSA) electrolyte, kept at room temperature, and cycled several times at 50 mV/s between 0 and 1.2 V until no further changes were observed in the cyclic voltammograms (CVs). Additional cycling at 10 mV/s was carried out. All potentials were measured with respect to a sealed reference hydrogen electrode (RHE)[24,25] that was made from 1 M TFMSA and separated from the electrochemical cell by a fine frit. For the oxygen reduction studies, the electrode was immersed in oxygen-saturated (Med-Tech Gases Inc.) electrolyte, and potentiodynamic polarization curves were recorded for potentials between 1.2 and 0.3 V at a scan rate of 25 mV/s and for rotation rates of 400, 625, 900, 1225, 1600, and 2500 rpm. Kinetic measurements of the ORR in terms of the Tafel parameters and kinetic currents were made according to numerous published approaches for analysis of the RDE data.[26,27] All electrochemical measurements were performed at room temperature with an RDE setup from Pine Instruments connected to an Autolab (Ecochemie Inc., model PGSTAT 30) potentiostat. As the kinetic data for all the rotation rates were the same, only 1225 rpm results are shown in the figures.

The choice of TFMSA as electrolyte was based on its low susceptibility for anion adsorption[28,29] and excellent transport properties of protons and dissolved oxygen.[30-34] TFMSA has a chemical structure close to the current state-of-the-art polymer electrolyte membranes belonging to the perfluorinated sulfonic acid family (such as Nafion from DuPont, Wilmington, DE).

Physicochemical characterization.—XRD measurements were made on the high-resolution X-18A beam line at the National Synchrotron Light Source (NSLS) at Brookhaven National Laboratory. A previous characterization of the 3:1 PtM/C composition[35] showed the existence of an fcc metallic phase with an average particle size of *ca.* 4 nm. Line broadening analysis of the primary XRD peak ⟨111⟩ was conducted using the Scherrer treatment of the data. The data were first fit to an indexing program, which allowed accurate measurement of the linewidths at half maximum. These widths were then used to obtain the particle sizes. Due to the high collimation of the synchrotron beam, corrections for beam deviations in the instrument were considered negligible.

X-ray absorption near-edge structure (XANES) data from *in situ* X-ray absorption spectroscopy (XAS) were measured. The objective was to verify the nominal atomic ratios as well as the nature of alloying, especially when the differences in the line shifts of the XRD patterns between Pt and Pt alloy electrocatalysts were very small. Further, the Pt d-band vacancy/atom was also determined from the relative areas under the Pt L_3 and L_2 edges for all the Pt and Pt alloy compositions. The methodology for analysis of the XANES spectrum followed that of Wong *et al.*[36] The procedure for determining the Pt d-band vacancy concentration was initially developed by Mansour *et al.*,[37,38] and the methodology has been applied to the study of electrocatalysis by Mukerjee *et al.*[4,12]

A special *in situ* spectroelectrochemical cell (described in detail elsewhere)[39] was used. Transmission mode XAS measurements were performed at beam line X-11 A at the NSLS on working electrodes in a fully flooded state. Data were collected at the Pt L, L_3, and L_2 edges, and at the K edges of the alloying metal transmission mode. Incident transmission and reference ion chambers were used (see Ref. 19).

Results and discussion.—The Pt:Co ratio in the electrocatalyst (Table I) was determined from the edge jumps at the Pt L_3 and Co K edges by methodologies described elsewhere.[35] The atomic ratios determined by XANES were in good agreement with approximate compositions projected from our preparation methodology. The XANES spectra were measured *in situ* for catalysts in 1 M $HClO_4$ at 0.54 V *vs.* RHE. This is the double layer region, where there is no

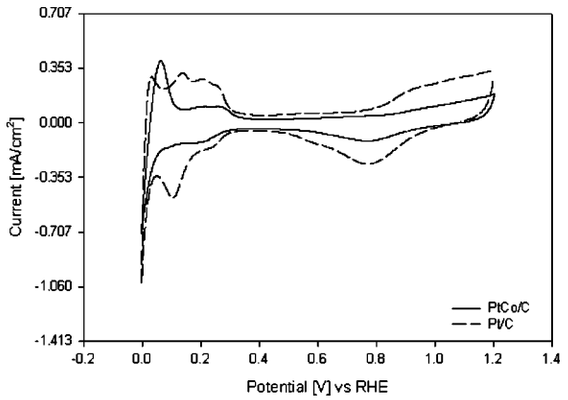

Figure 1. CVs at 50 mV/s sweep rate for Pt/C (--) and PtCo/C (—) on GC disk electrode in oxygen-free 1 M TFMSA at room temperature. Current densities are based on the electrode geometric area.

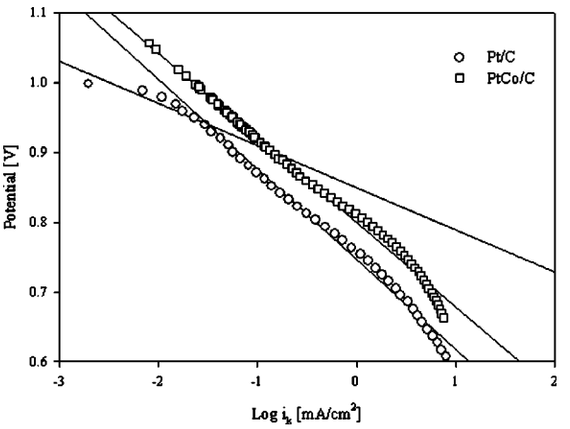

Figure 3. Tafel plots for ORR over Pt/C (○) and PtCo/C (□) in 1 M TFMSA at room temperature. Rotation rate is 1225 rpm and cathodic sweep rate is 25 mV/s.

interference from anionic adsorption or the redox processes associated with hydrogen deposition or evolution and oxygen reduction.

The Pt d-band vacancy numbers were derived from analysis of the Pt L_3 and L_2 white lines of XANES. The L_2 and L_3 lines are due to excitations of electrons to the empty Fermi level. Increases in the L_3 and L_2 white line peaks imply an increase in the d-band vacancy number or, equivalently, to a decreasing d-band occupancy. A detailed description of this methodology is given in Ref. 12 and the references therein. The Pt d-band occupancies as evaluated from the Pt L_3 and L_2 edge lines are given in Table I, along with the Pt:Co ratio. The table shows an increase in d-band vacancies as measured at Pt atoms upon alloying with Co.

XANES offers the ability to monitor the extent of alloying and the structure of the active surface. Two sets of PtCo/C catalysts were prepared: (*i*) acid washed in 1 M $HClO_4$ for 48 h at room temperature and (*ii*) unwashed. The acid washing step was followed by rinsing with deionized water to ensure the removal of any nonalloyed Co from the surface of the carbon support prior to electrode fabrication. The electrodes were held at 0.9 V *vs.* RHE while XANES spectra were recorded at the Pt L_3 and the Co K edges over periods of 6-10 h. For the unwashed samples, analysis of the Co K edge (details in Ref. 19) showed clear evidence of changes in the surface oxidation environment around the Co. For the electrode containing the washed catalyst, no variation was observed in the Co K edge XANES even after polarizing at 0.9 V for 9 h. For both the washed and unwashed alloy electrodes, no changes were detected at the Pt L_3 edge after polarizing at 0.9 V for 9 h. Further details are given in Ref. 19. These observations are consistent with an alloy catalyst structure with an outer layer of pure Pt, the Pt skin, as was proposed in Ref. 35.

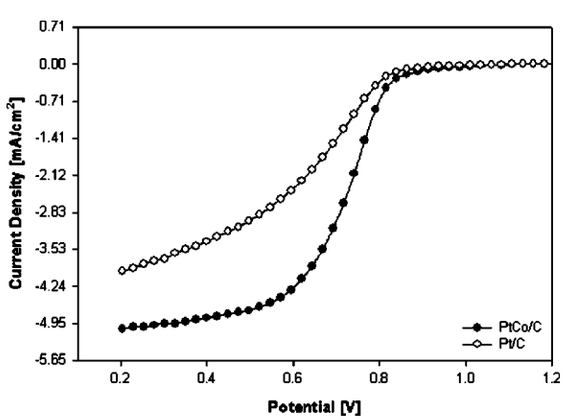

Figure 2. Disk current densities at 1225 rpm obtained during cathodic sweep showing ORR over Pt/C and PtCo/C in 1 M TFMSA at room temperature.

Cyclic voltammetry.—Figure 1 shows the steady-state CVs at 50 mV/s for Pt and PtCo catalyst particles supported on Vulcan XC-72R carbon with a metal loading of 14 μg metal/cm^2 in oxygen-free 1 M TFMSA. The carbon-supported Pt particles probably contain some low-index surface crystal planes, but detailed surface structural information cannot be inferred because the hydrogen adsorption/desorption features in CVs between 0 V and 0.4 V *vs.* RHE are different from those of the CVs of bulk polycrystalline Pt electrodes which have identifiable low-index surface plane features. The voltammetry curves of Pt and PtCo in Fig. 1 show a difference in the onset of oxide formation on Pt (accepted as Pt-OH), with PtCo/C exhibiting significantly less oxide formation in the >0.8 V range. This correlates with the increase in Pt 5d band vacancy concentration for the Pt skin on the alloy.

Oxygen reduction kinetics.—Figure 2 shows the disk current density obtained for Pt/C and PtCo/C supported on GC substrates in 1 M TFMSA at 1225 rpm during a cathodic sweep through the ORR range. The metal geometric loading was 14 μg/cm^2. The PtCo shows significantly improved ORR currents. The diffusion-corrected kinetic current Tafel plots are shown in Fig. 3. As seen in Fig. 3, both Pt/C and PtCo/C have Tafel slopes of around 120 mV dec^{-1} in the 0.8-0.9 V range. Traditionally, Langmuirian kinetics is used to explain the ~120 mV dec^{-1} slope below 0.8 V, whereas the ~60 mV dec^{-1} Tafel slope beyond 0.8 V, observed over a short range for Pt/C, is explained assuming oxygen adsorption under Temkin conditions in the presence of surface Pt-OH poison. However, these Tafel plots are complex, and it is likely that the electrode potential dependence of the activation energy for the first step plays a role in the observed curvature.[3] Further details of the kinetic measurements of the ORR in terms of the Tafel parameters and kinetic

Table II. Measured electrode potentials at different current densities for oxygen reduction over Pt/C and PtCo/C in 1 M TFMSA determined using RDE. Corresponding Tafel plots are in Fig. 3.

Electrocatalyst[a]	$V_{0.01\ mA/cm2}$ (mV)	$V_{0.1\ mA/cm2}$ (mV)	$V_{0.2\ mA/cm2}$ (mV)	Tafel slope (mV/dec)
Pt/C	0.979	0.872	0.833	~60/~120
PtCo/C	1.049	0.922	0.881	~120

[a] Metal loading on GC RDE, 14 μg/cm^2.

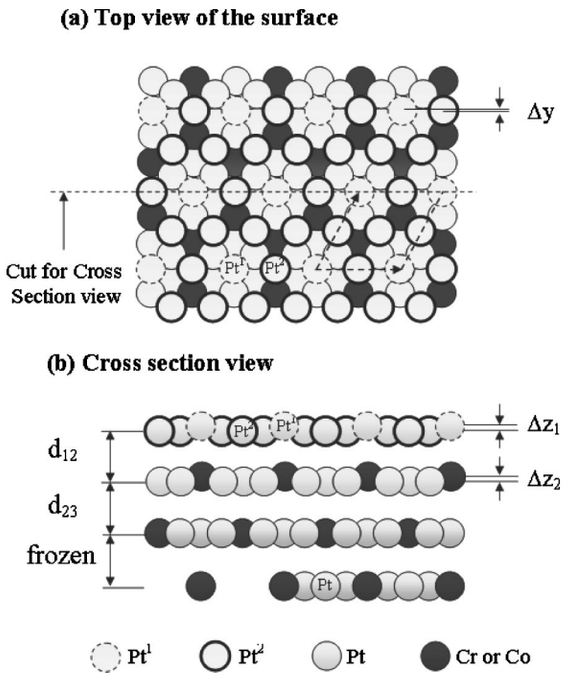

Figure 4. Two views of slab model used to study $Pt_3Co(111)$ and $Pt_3Cr(111)$ surfaces. d_{12}, d_{13}, Δy, Δz_1, and Δz_2 values are given in Table III. The (2×2) unit cell used for the calculations is shown with dashed lines in (a), and (b) is a view following the cut section represented in (a).

currents are given in Ref. 17. The kinetic parameters found from the Tafel plots given in Fig. 3 are summarized in Table II. Clearly, for a given current density, PtCo/C has a higher potential than Pt/C. The illustrative values in Table II show that at various current densities the PtCo/C overpotential is about 50-70 mV positive of that for Pt/C. This is consistent with previously published reports comparing similar electrocatalysts in RDE and polymer electrolyte membrane fuel cells.[4,9,12,23,40-42] The correlation of fuel cell potential and Pt oxidation with d-band vacancies has also been noted in Ref. 4, 12, 40, and 41.

Theoretical

Methodology.—Model to calculate the reversible potential shift.—The platinum alloying effect on the reversible potential of OH_{ads} formation from H_2O_{ads} was studied with a model using changes in surface adsorption bond strengths;[43] this model was also used in the Pr_3Cr study of Ref. 11. In this approach, the relationship between the Gibbs free energy for a reduction reaction and the reversible potential, U°

Table III. Calculated distances, *d* (Å), displacements, Δ*z* (Å) and Δ*y* (Å), and changes from bulk, Δ (%), for four-layer slab model of Pt(111) and for Pt skins on three-layer slabs of $Pt_3Cr(111)$ and $Pt_3Co(111)$. Parameters are illustrated in Fig. 4.

	One layer of Pt on three layers of					
	Pt(111)		$Pt_3Cr(111)$		$Pt_3Co(111)$	
d_{12}	2.33	1.3%	2.32	2.2%	2.32	2.6%
d_{23}	2.29	−0.4%	2.24	−1.3%	2.21	−2.2%
d_{34}	2.30	Frozen	2.27	Frozen	2.26	Frozen
Δz_1	0.00		0.06		0.10	
Δz_2	0.00		0.06		0.09	
Δy	0.00		0.02		0.02	

$$U^\circ = -\Delta G^\circ/nF \quad [10]$$

is used, where ΔG° (eV) is the free Gibbs energy change for the reaction, n is the number of electrons in the reaction, and F is the Faraday constant. By fitting a number of reactions involving H_xO_y, ΔG° can be well approximated by the reaction energy, E_r, plus constant terms

$$U^\circ = -(E_r/nF) - 4.6 + c \quad [11]$$

The −4.6 V contribution comes from the fact that the energy of an electron at 0 V on the electrochemical scale is −4.6 eV on the physical (vacuum) scale,[44] which is the one in which the quantum calculations take place. The constant c represents the missing $P\Delta V$ and $T\Delta S$ energy contributions to the Gibbs energy. It is nearly constant for reactions involving O-H bonds in acid solution and can be determined by fitting experimental U°.[43] However, c is not needed when comparing a reaction in different environments to find new reversible potentials, as long as $P\Delta V - T\Delta S$ remains almost constant. Thus, when the reversible potential for OH reduction in acid solution is known, the reversible potential of OH_{ads} formation from H_2O_{ads} on a catalyst surface by the reaction

$$(\text{catalyst})\text{-OH} + H^+_{aq} + e^-(U^\circ) \leftrightarrows (\text{catalyst})\text{-OH}_2 \quad [12]$$

can be estimated as the reversible potential of OH formation from H_2O in aqueous acid solution plus the change in reaction energy for forming OH_{ads} from H_2O_{ads} on a catalyst surface. When the catalyst is a platinum surface, the reversible potential is then given as

$$\begin{aligned} U^\circ(\text{on Pt}_{slab}) &= U^\circ \text{ (in aqueous acid solution)} - \Delta E_r/nF \\ &= U^\circ \text{ (in aqueous acid solution)} \\ &\quad + [E_{ads}(H_2O)_{Pt} - E_{ads}(OH)_{Pt}]/nF \end{aligned} \quad [13]$$

From the known reversible potential for OH_{ads} formation from H_2O_{ads} on a specific catalyst, the shift of the reversible potential on two unlike catalyst compositions, for example, on pure Pt and on an alloy surface, is given by

$$\begin{aligned} \Delta U^\circ &= U^\circ \text{ (on alloy surface)} - U^\circ\text{(on Pt surface)} \\ &= [E_{ads}(OH)_{Pt} - E_{ads}(OH)_{alloy} - E_{ads}(H_2O)_{Pt} \\ &\quad + E_{ads}(H_2O)_{alloy}]/nF \end{aligned} \quad [14]$$

Equation 14 is the model used in this work to calculate the effect of alloying Pt with Co atoms on the onset potential for forming the OH_{ads}. This adsorbed specie is believed to be a poison that is responsible for at least part of the high overpotential for O_2 reduction on cathodes in fuel cells.[1,5,7,10,12] In summary, with this model only the knowledge of the adsorption energies of OH and H_2O on two unlike catalyst surfaces is required for estimating the shift in reversible potential for OH_{ads} formation.

Periodic calculations.—The Vienna Ab Initio Simulation Program (VASP)[45-48] was used for calculating H_2O and OH adsorption bond strengths. VASP performs an iterative solution of the Kohn-Sham equation of local-density-approximation theory in a plane-wave basis. The self-consistent solutions, corresponding to the electronic ground states, are determined via an iterative unconstrained band-by-band matrix-diagonalization scheme based on a residual minimization method.[48,49] The electron-ion interaction is described by optimized ultrasoft pseudopotentials.[50] To take into account the nonlocality in the exchange-correlation functional, the generalized gradient approximation as proposed by Perdew and Wang (PW91)[51] was used. Brillouin zone integrations were performed using Monkhorst-Pack grids[52] with a generalized Gaussian smearing[53] of $\sigma = 0.2$ eV for integration in reciprocal space. Results were checked for convergence with respect to the number of k-points as well as with respect to the energy cutoff for the plane waves. The planes wave energy cutoff was optimized at 400 eV for all calculations. The k-point meshes used for all the (2×2) translational primitive

Table IV. Calculated results for OH adsorption at 0.25 ML coverage on four-layer slab model of Pt(111) and on Pt skins on $Pt_3Cr(111)$ and $Pt_3Co(111)$.

	OH adsorption on Pt top sites					
	Site	E_{ads}	ΔE_{ads}	d(Pt-O)	d(O-H)	α1
Pt(111)	Pt	2.37		2.00	0.98	106.9
Pt skin on Pt_3Cr	Pt^1	2.22	−0.15	2.00	0.98	103.5
	Pt^2	2.24	−0.13	2.01	0.98	105.3
Pt skin on Pt_3Co	Pt^1	2.25	−0.13	2.00	0.98	106.1
	Pt^2	2.20	−0.17	2.02	0.98	106.7

E_{ads} (eV) are the adsorption energies of OH; d(Pt-O) and d(O-H) are the interatomic distances (Å); α1 is the surface O-H angle (deg); and ΔE_{ads} are the adsorption energy decreases relative to the Pt(111) slab.

cells were $(5 \times 5 \times 1)$. These choices guaranteed a sufficient energy convergence with respect to the energy cutoff and the number of *k*-points.

The local-spin-density functional calculations performed by Lu *et al.*[54] showed that spin polarization in the calculations had a crucial influence on the structure stability of Pt_3X alloys when X = Sc, Ti, V, Cr, Mn, Fe, Co, Ni, and Cu and that many of the Cu_3Au-type ordered alloys are magnetic.[55-66] Therefore, to take into account the effects of spin polarization, all calculations were done with the spin-polarized version of VASP.

Surfaces were represented by slabs composed of four layers of substrate separated by six layers of vacuum (~13.5 Å). Adsorbates were introduced on only one side of the slab. Structures were found using a quasi-Newton algorithm to minimize the Hellmann-Feynman forces acting on atoms.[67] The two topmost metal layers with adsorbates were allowed to relax, while the two deeper layers were kept frozen in the bulk configuration.

Results and discussion.—Modeling of the $Pt_3Co(111)$ surface.—The thermodynamic stability of Pt on the first layer was found in the theoretical studies of Ruban *et al.*[68] and of Christensen *et al.*,[69] who reported segregation energies of 0.46 and 0.52 eV/atom, respectively, corresponding to a strong antisegregation of Co in the first layer of the alloy surface. The segregation energy was defined as the difference in total energies of the system with impurity in a surface layer and in the bulk. Results from our XANES investigation of Pt_3Co alloy surface also show Pt segregation in the first layer of the Pt_3Co surface. To take the Pt segregation into account, we have used a slab composed of one pure Pt layer on three atom layers of ordered $Pt_3Co(111)$, leading to Pt concentrations of 100 and 75% in the top and underlying layers, respectively (see Fig. 4). The minority $L1_0$ phase observed earlier[12] is not treated theoretically. Due to the presence of Co atoms in the deeper layers of this model, there are two different surface Pt positions denoted Pt^1 and Pt^2. Pt^1 has three Pt atoms as nearest neighbors located in the second layer, and Pt^2 has two Pt atoms and one Co atom as nearest neighbors in the second layer (see Fig. 4).

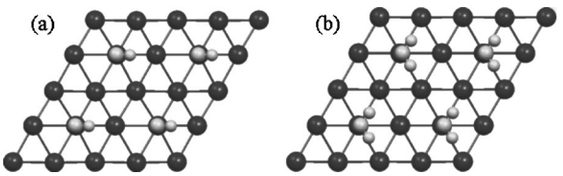

Figure 5. (a) OH and (b) H_2O adsorption orientations at top sites on Pt(111), and on the Pt skins on Pt_3Cr or Pt_3Co. For clarity, only the first layer is shown.

Structure results.—The Pt_3Co bulk lattice constant in the $L1_2$ phase was calculated to be 3.91 Å, which is 0.06 Å greater than the experimental bulk crystal value of 3.85 Å.[12] As previously observed experimentally, the calculated lattice parameter of bulk Pt_3Co is contracted 2.0% from that of Pt bulk, which was calculated in a previous study to be 3.99 Å[11] (the experimental contraction of the lattice constant is 1.9%).[12] Atoms in the bottom two layers below the surface used for adsorption calculations were frozen in the calculated bulk geometry. Table III summarizes the optimized geometrical results for the $Pt_3Co(111)$ surface model. Some results for Pt(111) and Pt skin on $Pt_3Cr(111)$ from Ref. 11 are also included for comparison. As Table III shows, an expansion of about 2.6% of the distance between the first and the second layer and a contraction of about 2.2% between the second and third layer of the Pt_3Co surface model were found. These results correlate with the previous geometrical investigation of the Pt skin on $Pt_3Cr(111)$ in Ref. 11, where an expansion of 2.2% and a contraction of about 1.3% were predicted (see Table III). The amplitudes of these relaxations are greater for the alloy surfaces than for Pt(111). These surface reconstruction features can be attributed to the formation of very strong Pt-Cr and Pt-Co bonds. A similar behavior was also observed for Pt skin-covered alloys in the theoretical study of the $Pt_{80}Fe_{20}$ surface of Hirschl *et al.*[70]

OH and H_2O adsorption.—Each calculation of OH and H_2O on the Pt skin on $Pt_3Co(111)$ was performed with a (2×2) surface unit cell to model 0.25 monolayer (ML) coverage, and the two topmost surface layers were allowed to relax with their attached adsorbates while the two other deepest layers were kept frozen in the calculated bulk configuration (see Fig. 4). Adsorption energies, E_{ads}, per OH or H_2O were calculated using

$$E_{ads} = E(OH_n) + E(\text{slab}) - E(OH_n - \text{slab}) \quad [15]$$

In this equation, OH_n is OH or H_2O and $E(OH_n)$, E(slab), and $E(OH_n\text{-slab})$ are the respective calculated energies of the free adsorbates, the slab, and the slab with the adsorbates. In the previous

Table V. Calculated results for H_2O adsorption at 0.25 ML coverage on four-layer slab model of Pt(111) and on Pt skins on $Pt_3Cr(111)$ and $Pt_3Co(111)$.

	H_2O adsorption on Pt top sites						
	Site	E_{ads}	ΔE_{ads}	d(Pt-O)	d(O-H)	α2	α3
Pt(111)	Pt	0.25		2.43	0.98	105.3	91.2
Pt skin on Pt_3Cr	Pt^1	0.14	−0.09	2.71	0.98	104.6	80.5
	Pt^2	0.21	−0.02	2.57	0.98	104.9	94.0
Pt skin on Pt_3Co	Pt^1	0.14	−0.09	2.64	0.98	104.5	85.3
	Pt^2	0.21	−0.02	2.56	0.98	104.6	91.8

E_{ads} (eV) are the adsorption energies of H_2O; d(Pt-O) and d(O-H) are the interatomic distances (Å); α2 is the H-O-H angle (deg), and α3 is the angle (deg) between the H_2O plane and a perpendicular direction to the surface; and ΔE_{ads} are adsorption energy decreases relative to the Pt(111) slab.

investigation of OH and H_2O adsorption on the unalloyed Pt(111) and on the Pt skin on $Pt_3Cr(111)$ alloy, it was shown that OH and H_2O adsorb preferentially on top sites.[11] Therefore, in this study only the top adsorption sites are used. Whereas on the Pt(111) surface there is only one possible top adsorption site, on the Pt skin on $Pt_3Co(111)$ or on $Pt_3Cr(111)$ there are two different possible top adsorption sites, Pt^1 and Pt^2, due to the Co or Cr atoms below.

Results for OH adsorption on the three different catalyst surfaces are summarized in Table IV. The OH adsorption energies are less on the Pt skin on $Pt_3Co(111)$ and $Pt_3Cr(111)$ than on Pt(111). The differences are 0.13 and 0.17 eV for the Pt skin on Pt_3Co and 0.15 and 0.13 eV for the Pt skin on Pt_3Cr for adsorption on Pt^1 and Pt^2 sites, respectively. The 0.25 ML OH-covered Pt(111) surface and the 0.25 ML OH-covered Pt skins on the alloys are similar, as shown in Fig. 5a, where, for clarity, only the first surface metal layer is shown. For the three surfaces, the Pt-O and O-H bond strengths remain almost unchanged at about 2.00 and 0.98 Å, respectively. The Pt -O-H angle undergoes small variations. For the three catalyst surfaces, the most stable orientation of OH, shown in Fig. 5a, has the O-H axis inclined toward a bridge site in the direction of a Pt atom.

The corresponding energies and structure data for H_2O adsorption are summarized in Table V. Very close results (energetic as well as geometric) for H_2O adsorption on the Pt skin on the $Pt_3Co(111)$ and on the $Pt_3Cr(111)$ were calculated. There is a small decrease in the H_2O adsorption energies on both Pt skin surfaces relative to Pt(111). The energy variation for both surfaces is 0.09 and 0.02 eV on the Pt^1 and Pt^2 positions, respectively. As for OH, adsorbed H_2O has the same overall structure on the three catalyst surfaces after optimization, as shown in Fig. 5b. Again, for clarity, only the first surface metal layer is shown.

Potential shift.—Using the most stable OH and H_2O adsorption energies from Tables IV and V in Eq. 5, a positive potential shift in reversible potential for forming OH_{ads} from H_2O_{ads} of about $\Delta U^\circ = 0.08$ V was calculated for the Pt skin on the $Pt_3Co(111)$ alloy surface, relative to Pt(111). This is 0.03 V less than on the Pt skin on the $Pt_3Cr(111)$ surface. This positive shift correlates with the experimental voltammetry of Pt and Pt_3Co in Fig. 1, which clearly shows a positive shift of the onset potential for forming OH_{ads} on the alloy relative to the Pt catalyst at around 0.8 V. It also agrees with the positive onset potential shift observed in the study of the annealed Pt_3Co alloy surface of Stamenkovic *et al.*[5]

Conclusion

This work reports an experimental and theoretical attack on understanding the activity toward O_2 reduction, in acid, of the Pt_3Co alloy relative to the Pt catalyst. From the results, the ORR clearly depends significantly on the surface composition and structure. Alloying Pt with transition metals such as Co and Cr[11] leads to an enhancement of the ORR. The experimental and theoretical approaches suggest that this improvement can be attributed to a positive shift of the onset potential for forming OH_{ads} on the alloy relative to the Pt catalyst, thereby allowing O_2 to adsorb at higher potentials and reducing the overpotential for O_2 reduction.

Acknowledgments

J.R. and A.B.A. are pleased to acknowledge support for this work by the U.S. Department of Energy through a subcontract from U.T.C. Fuel Cells. V.S.M. and S.M. gratefully acknowledge support from the Army Research Office through a Single Investigator and Multi-University Research Initiative (MURI) grants. S.M. is also grateful to the U.S. Department of Energy, Materials Science Division, for providing the NSLS at Brookhaven National Laboratory, Upton, NY (beam line X-11A).

References

1. N. M. Markovic and P. N. Ross, *Surf. Sci. Rep.*, **45**, 117 (2002).
2. A. B. Anderson and T. V. Albu, *J. Electrochem. Soc.*, **147**, 4229 (2000).
3. R. A. Sidik and A. B. Anderson, *J. Electroanal. Chem.*, **528**, 69 (2002).
4. S. Mukerjee, S. Srinivasan, M. P. Soriaga, and J. McBreen, *J. Phys. Chem.*, **99**, 4577 (1995).
5. V. Stamenkovic, T. J. Schmidt, P. N. Ross, and N. M. Markovic, *J. Phys. Chem. B*, **106**, 11970 (2002).
6. A. B. Anderson, *Electrochim. Acta*, **47**, 3759 (2002).
7. N. M. Markovic, H. A. Gasteiger, B. N. Grgur, and P. N. Ross, *J. Electroanal. Chem.*, **467**, 157 (1999).
8. N. M. Markovic, T. J. Schmidt, B. N. Grgur, H. A. Gasteiger, R. J. Behm, and P. N. Ross, *J. Phys. Chem. B*, **103**, 8568 (1999).
9. S. Mukerjee and S. Srinivasan, *J. Electroanal. Chem.*, **357**, 201 (1993).
10. F. A. Uribe and T. A. Zawodzinski, *Electrochim. Acta*, **47**, 3799 (2002).
11. J. Roques and A. B. Anderson, *J. Electrochem. Soc.*, **151**, E85 (2004).
12. S. Mukerjee, S. Srinivasan, and M. P. Soriaga, *J. Electrochem. Soc.*, **142**, 1409 (1995).
13. V. M. Jalan and C. L. Bushnell, U.S. Pat. 4,137,372 (1979).
14. V. M. Jalan, Eur. Pat. Appl. 165,024 (1985).
15. D. A. Landsman and F. J. Luczak, Belg. Pat. 889,143 (1981).
16. P. Stonehart, M. Watanabe, N. Yamamoto, T. Nakamura, N. Hara, and K. Tsurumi, Jpn. Pat. 04,141,236 (1992).
17. V. S. Murthi, R. C. Urian, and S. Mukerjee, *J. Electrochem. Soc.*, Submitted.
18. S. Mukerjee *J. Appl. Electrochem.*, **20**, 537 (1990).
19. S. Mukerjee and R. C. Urian, *Electrochim. Acta*, **47**, 3219 (2002).
20. H. S. Lee, X. O. Yang, J. McBreen, and C. Xiang, in U.S., (Brookhaven Science Associates, USA). Us 2000, 11.
21. U. S. Paulus, T. J. Schmidt, H. A. Gasteiger, and R. J. Behm, *J. Electroanal. Chem.*, **495**, 134 (2001).
22. U. A. Paulus, A. Wokaun, G. G. Scherer, T. J. Schmidt, V. Stamenkovic, N. M. Markovic, and P. N. Ross, *Electrochim. Acta*, **47**, 3787 (2002).
23. U. A. Paulus, A. Wokaun, G. G. Scherer, T. J. Schmidt, V. Stamenkovic, V. Radmilovic, N. M. Markovic, and P. N. Ross, *J. Phys. Chem. B*, **106**, 4181 (2002).
24. S. Gong, J. Lu, and H. Yan, *J. Electroanal. Chem.*, **436**, 291 (1997).
25. F. G. Will, *J. Electrochem. Soc.*, **133**, 454 (1986).
26. S. L. Gojkovic, S. K. Zecevic, and R. F. Savinell *J. Electrochem. Soc.*, **145**, 3713 (1998).
27. S. K. Zecevic, J. S. Wainright, M. H. Litt, S. L. Gojkovic, and R. F. Savinell *J. Electrochem. Soc.*, **144**, 2973 (1997).
28. P. J. Hyde, C. J. Maggiore, A. Redondo, S. Srinivasan and S. Gottesfeld *J. Electroanal. Chem. Interfacial Electrochem.*, **186**, 267 (1985).
29. M. A. Habib and J. O. Bockris, *Compr. Treatise Electrochem.*, **1**, 135 (1980).
30. E. Yeager, M. Razaq, D. Gervasio, A. Razaq, and D. Tryk, in *Structural Effects in Electrocatalysts and Oxygen Electrochemistry*, D. Scherson, D. Tryk, M. Daroux, and X. Xing, Editors, PV 92-11, p. 440, The Electrochemical Society Proceedings Series, Pennington, NJ (1992).
31. E. Yeager, M. Razaq, D. Gervasio, A. Razaq, and D. Tryk, *J. Serb. Chem. Soc.*, **57**, 819 (1992).
32. E. Yeager, Report LBL-29696, Department of Chemistry, Case Western Reserve University, Cleveland, OH (1990).
33. E. Yeager, *Electrochim. Acta*, **29**, 1527 (1984).
34. M. A. Enayetullah, Ph.D. Thesis, Case Western Reserve University, Cleveland, OH (1986).
35. J. McBreen and S. Mukerjee, *J. Electrochem. Soc.*, **142**, 3399 (1995).
36. J. Wong, F. W. Lytle, R. P. Messmer, and D. H. Maylotte, *Phys. Rev. B*, **30**, 5596 (1984).
37. A. N. Mansour, J. W. Cook, Jr., D. E. Sayers, R. J. Emrich, and J. R. Katzer, *J. Catal.*, **89**, 462 (1984).
38. A. N. Mansour, J. W. Cook, Jr., and D. E. Sayers, *J. Phys. Chem.*, **88**, 2330 (1984).
39. J. McBreen, *Phys. Electrochem.*, **1995**, 339.
40. S. Mukerjee, *Catalysis and Electrocatalysis at Nanoparticle Surfaces*, A. Wieckowski, E. R. Savinova and C. G. Vayenas, Editors, Marcel Dekker, New York (2003).
41. S. Mukerjee and J. McBreen, in *Electrode Processes*, A. Wieckowski and K. Itaya, Editors, PV 96-8, p. 421, The Electrochemical Society Proceeding Series, Pennington, NJ (1996).
42. R. R. Adzic, *Electrocatalysis*, J. Lipkowski and P. N. Ross, Editors, p. 197, Wiley VCH, Inc., Weinheim (1998).
43. A. B. Anderson and T. V. Albu, *J. Am. Chem. Soc.*, **121**, 11855 (1999).
44. J. O. Bockris and S. U. M. Khan, *Surface Electrochemistry: Molecular Level Approach*, p. 319, Plenum, New York (1993).
45. G. Kresse and J. Hafner, *Phys. Rev. B*, **47**, 558 (1993).
46. G. Kresse and J. Hafner, *Phys. Rev. B*, **49**, 14251 (1994).
47. G. Kresse and J. Furthmüller, *Phys. Rev. B*, **54**, 11169 (1996).
48. G. Kresse and J. Furthmüller, *Comput. Mater. Sci.*, **6**, 15 (1996).
49. D. M. Wood and A. Zunger, *J. Phys. A*, **18**, 1343 (1985).
50. G. Kresse and J. Hafner, *J. Phys.: Condens. Matter*, **6**, 8245 (1994).
51. J. P. Perdew and Y. Wang, *Phys. Rev. B*, **45**, 13244 (1992).
52. H. J. Monkhorst and J. D. Pack, *Phys. Rev. B*, **13**, 5188 (1976).
53. M. Methfessel and A. T. Paxton, *Phys. Rev. B*, **40**, 3616 (1989).
54. Z. W. Lu, B. M. Klein, and A. Zunger, *Phys. Rev. Lett.*, **75**, 1320 (1995).
55. R. B. Patel, A. J. Liddiard, and M. D. Crapper, *J. Phys.: Condens. Matter*, **6**, 9973 (1994).
56. S. B. Burke, B. D. Rainford, D. E. G. Williams, P. J. Brown, and D. A. Hukin, *J. Magn. Magn. Mater.*, **15**, 505 (1980).
57. D. E. G. Williams and A. Jezierski, *J. Magn. Magn. Mater.*, **59**, 41 (1986).
58. H. Maruyama, F. Matsuoka, K. Kobayashi, and H. Yamazaki, *J. Magn. Magn. Mater.*, **140**, 43 (1995).
59. A. Borgschulte, D. Zur, D. Menzel, and J. Schoenes, *Phys. Rev. B*, **66**, 144421 (2002).

60. S. J. Pickart and R. Nathans, *J. Appl. Phys.*, **34**, 1203 (1963).
61. M. Maret, M. Albrecht, J. Köhler, R. Poinsot, C. Ulhaq-Bouillet, J. M. Tonnerre, J. F. Berar, and E. Bucher, *J. Magn. Magn. Mater.*, **218**, 151 (2000).
62. T. Tohyama, Y. Ohta, and M. Shimizu, *J. Phys.: Condens. Matter*, **1**, 1789 (1989).
63. M. Shirai, *Physica B*, **237**, 351 (1997).
64. Z. W. Lu, B. M. Klein, and H. T. Chau, *Phys. Rev. B*, **58**, 9252 (1998).
65. P. M. Oppeneer, V. N. Antonov, T. Kraft, H. Eschrig, A. N. Yaresko, and A. Y. Perlov, *J. Phys.: Condens. Matter*, **8**, 5796 (1996).
66. K. Iwashita, T. Oguchi, and T. Jo, *Phys. Rev. B*, **54**, 1159 (1996).
67. R. P. Feynman, *Phys. Rev.*, **56**, 340 (1939).
68. A. V. Ruban, H. L. Skriver, and J. K. Norskov, *Phys. Rev. B*, **59**, 15990 (1999).
69. A. Christensen, A. V. Ruban, P. Stoltze, K. W. Jacobsen, H. L. Skriver, J. K. Norskov, and F. Besenbacher, *Phys. Rev. B*, **56**, 5822 (1996).
70. R. Hirschl, F. Delbecq, P. Sautet, and J. Hafner, *Phys. Rev. B*, **66**, 155438 (2002).